

Lattice Boltzmann simulation of free surface flow impact on a structureE. Dinesh Kumar, S. A. Sannasiraj,^{*} and V. Sundar*Department of Ocean Engineering, Indian Institute of Technology Madras, Chennai 600036, India*

(Received 1 November 2018; published 11 February 2019)

Liquid impact on a rigid wall is a common feature in the context of marine structures, as most of them are exposed continuously to breaking waves. In the present paper, a comparison and analysis of the impact load estimates obtained from free surface lattice Boltzmann (LB) simulation with the experimental measurements from available literature have been reported. Initially, two-dimensional simulation of the dam break impact on the wall is performed with two different LB models: BGK-F1: a Bhatnagar-Gross-Krook (BGK) collision operator with the force scheme of Buick and Greated [*Phys. Rev. E* **61**, 5307 (2000)], and MRT-F2: a multiple relaxation time (MRT) operator with the force scheme of Guo *et al.* [*Phys. Rev. E* **65**, 046308 (2002)]. The pressure estimates obtained from BGK-F1 over MRT-F2 are closer to the measurements, though the other key parameters, such as the waterfront evolution and the free surface profile, have not shown significant variations. Furthermore, the three-dimensional dam break simulation has been performed using BGK-F1 for three test cases: (i) impact on a wall, (ii) impact on a rectangular obstacle, and (iii) impact on a tall tower. In all the test cases, the load estimates are in agreement with the experimental measurements.

DOI: [10.1103/PhysRevE.99.023308](https://doi.org/10.1103/PhysRevE.99.023308)**I. INTRODUCTION**

The flow due to the sudden release of a water column, commonly known as a dam break, is a very violent scenario. It is of practical importance to understand the behavior of pressure fluctuations and their impact on a wall, especially in the context of coastal, marine, and hydraulic structures. The flow that occurs after the collapse of a dam is driven mainly by gravity, and it can be categorized into the class of liquid impact problems in which the relative motion between the plane of impact and the liquid mass has a constant acceleration [1]. Several experimental [2–5], theoretical [6,7], and numerical [8,9] studies have attempted to understand flow dynamics on the fluid structure interaction problem.

In general, the flow field can be modeled in three different ways: (i) the shallow-water or depth-integrated model (Boussinesq equation), (ii) the potential flow model (Laplace equation), and (iii) the nonhydrostatic model [Navier-Stokes (NS) equation]. These model equations can be solved through traditional mesh-based schemes such as finite-difference, element, or volume methods, or particle methods such as smoothed particle hydrodynamics (SPH). The occurrence of flow separation due to high vertical velocities limits the application of the shallow-water model for violent scenarios such as a dam break or a wave overtopping, and in the same vein the potential flow model fails due to the assumption of flow being irrotational. The solution to the pressure-Poisson equation at each simulation time step is the major bottleneck involved in direct NS solvers [10]. Another challenging aspect is the requirement of an accurate representation of the free surface for complex problems, wherein processes such as splashing, mixing, and entrapment of one fluid with another tend to occur. Earlier, front-tracking [11], volume of fluid (VOF) [12],

and level set (LS) [13] schemes were utilized to capture or track the interface. Due to their Eulerian nature, VOF and LS schemes have been widely used, but they have their own advantages and disadvantages. The VOF method proves to be mass-conservative throughout the computational domain, but the calculation of the surface normal is not so trivial. On the other hand, LS schemes provide a better approximation for the surface normal, but they lack a mass-conservation property. The improvements made in both schemes to overcome their respective drawbacks results in a loss of simplicity.

A simple and accurate representation of free surface flow modeling has been achieved with the development of the lattice Boltzmann method (LBM) as an alternative to traditional NS-based fluid flow solvers. The LBM belongs to the class of grid-based particle methods [10] wherein mesh is not required and instead uniform grids are adopted. The task of obtaining a solution to the pressure-Poisson equation is not required, and thus the major time-consuming task has been alleviated. Furthermore, the explicit nature of the LBM is found to be more suitable for modern computers in terms of parallelization [10].

The VOF-based free surface LB model has been applied to various problems, such as metal foaming [14], dam break [15], particle suspension flows [16], and droplet motion [17]. In addition to VOF-based models, the kinematic boundary condition (KBC)-based free surface LB model has been proposed for water waves [18]. LB-KBC is not applicable for complex scenarios such as breaking or merging due to the fact that the interface parameter (the height function) is a single-valued function. Earlier free surface LB simulations [15,19] of dam break flow proved to be attractive and satisfactory, especially in the context of free surface representation, but the analyses of hydrodynamic parameters such as pressure have not been discussed in detail. In this context, the present study focuses on a detailed comparison and analysis of hydrodynamic estimates, such as pressure and total force, from the developed

^{*}sasraj@iitm.ac.in

LB model with three different experimental scenarios from the literature. These experiments [5,20,21] were carried out to understand the nature of impact in the context of water waves. Since the extension from two-dimensional (2D) to three-dimensional (3D) modeling is relatively easier in the LBM, 3D simulation has been carried out in the present study and the results are compared with the experimental measurements.

In what follows, the free surface LB model along with the boundary conditions are described in Sec. II. The simulation setup and the results are discussed in Sec. III, and Sec. IV summarizes with salient conclusions.

II. LATTICE BOLTZMANN MODEL FOR FREE SURFACE FLOWS

The continuity and incompressible Navier-Stokes equations govern the flow field. The LB model for the flow field is given by

$$f_i(\mathbf{x} + \mathbf{e}_i \Delta t, t + \Delta t) - f_i(\mathbf{x}, t) = \Lambda_{ij}(f_j^{\text{eq}} - f_j) + S_i, \quad (1)$$

where $f_i^{\text{eq}} = \omega_i \rho (1 + \frac{\mathbf{e}_i \cdot \mathbf{u}}{c_s^2} + \frac{(\mathbf{e}_i \cdot \mathbf{u})^2}{2c_s^4} - \frac{\mathbf{u} \cdot \mathbf{u}}{2c_s^2})$ is the equilibrium distribution function for the i th direction, with ω_i the lattice weights, \mathbf{e}_i the lattice velocity, c_s the sound speed ($c_s^2 = \frac{1}{3}$), and S_i the source term, including external forces, \mathbf{F} . The term Λ_{ij} represents the element in a collision matrix and for the Bhatnagar-Gross-Krook (BGK) operator $\Lambda_{ij} = \frac{1}{\tau}$, where τ is the relaxation time. The multiple relaxation time (MRT) collision operator is given by $\Lambda = \mathbf{M}^{-1} \mathbf{S} \mathbf{M}$, where \mathbf{S} is the diagonal relaxation matrix and \mathbf{M} is the moment matrix, which transforms the distribution function f_i from population to moment space and whose inverse \mathbf{M}^{-1} transforms the distribution function back to population space. The macroscopic flow variables such as density (ρ) and momentum ($\rho \mathbf{u}$) can be obtained by taking the moments of the distribution function [15,22,23].

Water is taken as a working fluid in the present study. Even though water is assumed to be an inviscid fluid for all practical purposes, the value of viscosity cannot be set to zero in the LBM. The lower viscosity results in higher Reynolds numbers, hence it is crucial to obtain an appropriate relaxation time within the stability limits (0.5, 2.0). Since the LBM is a quasi-incompressible flow solver, the condition $\Delta t \sim \Delta x^2$ must be satisfied to avoid compressibility effects, and this

results in an increase in the grid size [24]. In addition to this increase, the requirement of a uniform grid size for each direction results in a large mesh-size while one attempts to map an actual physical space. For example, if the length of the water tank is about a few meters and the representation of a vertical water column or surface wave of amplitude is a few centimeters, a grid size of $\Delta x \ll 1$ cm would be required to capture the interface, and thus the number of grid points along the horizontal axis would increase.

The choice of collision operators plays a major role in improving stability for large Reynolds numbers. Furthermore, to reduce the grid size and to improve the stability of the LB simulation simultaneously, three different approaches exist in the literature: (i) the large-eddy simulation (LES) [25], (ii) the viscous counteract force (VSC) approach [26], and (iii) the fractional step (FS) approach [27]. In VSC-LB and FS-LB, instead of the actual viscosity, an artificial viscosity has been introduced to solve for the flow field. With regard to the correction of the flow field for actual viscosity, in the case of FS-LB a fractional step solver for the first-order advection equation has been used, whereas VSC-LB treats part of the stress tensor as an external force. On the other hand, LES-LB corrects the relaxation time by computing the eddy viscosity. The LES-LB model have been successfully demonstrated in various turbulent flow scenarios, such as square jet flow [28], channel flow [25], and free surface flow [15]. Hence, to deal with large Reynolds numbers of $O(10^6)$ involved in the present case, the LES turbulence model has been incorporated (see Appendix A for details).

In the present study, gravity is the sole body force acting on the fluid particles, and other forces such as surface tension are neglected. Earlier studies on dam break flow [15,19] adopted a simple approach for gravity, $S_i = 3\omega_i \rho \mathbf{e}_i \cdot \mathbf{F}_b$ [22]. Later, an accurate scheme was proposed for unsteady flow that accounts for the contribution of body force on momentum and the influence of momentum and density on the spatial-temporal variation of the force [23]. In the model of Guo *et al.* [23], the representations of the source term S_i and the force term F_i are given by

$$S_i = \left[\mathbf{M}^{-1} \left(\mathbf{I} - \frac{1}{2} \mathbf{S} \right) \mathbf{M} \right] F_i, \quad (2)$$

$$F_i = \omega_i \left[\frac{\mathbf{e}_i - \mathbf{u}}{c_s^2} + \frac{\mathbf{e}_i \cdot \mathbf{u}}{c_s^4} \mathbf{e}_i \right] \cdot \mathbf{F}_b.$$

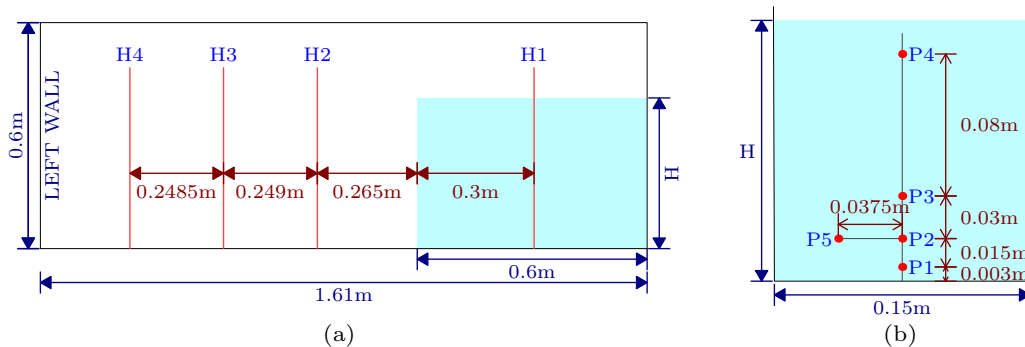


FIG. 1. (a) Initial dam break setup [5] and (b) the locations of pressure probes placed at the left wall. (a) Side view; (b) pressure probes at the left wall.

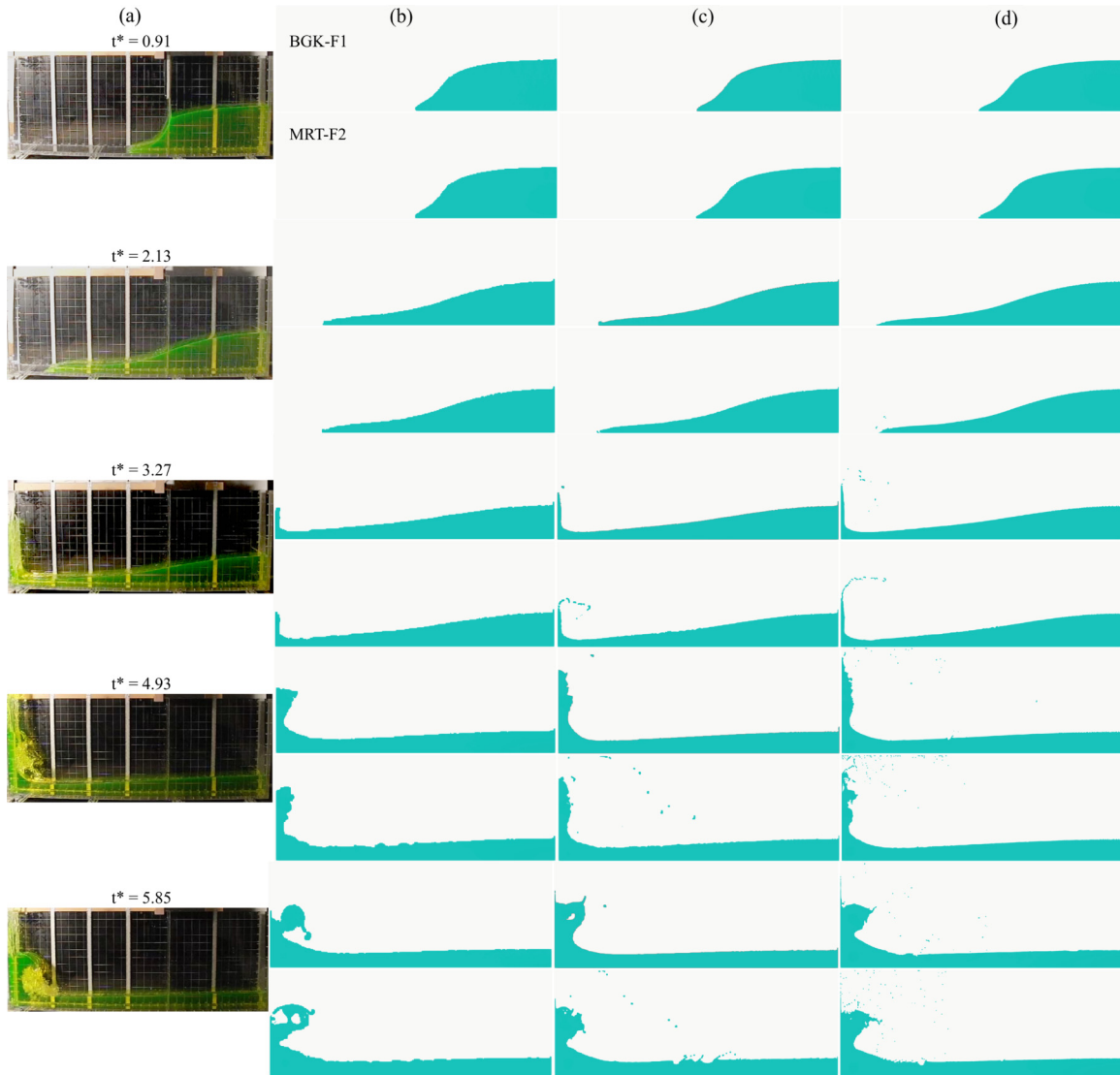


FIG. 2. Two-dimensional free surface evolution of BGK-F1 (first row) and MRT-F2 (second row) with experiments: (a) Ref. [5], $\Delta x = 0.005$ m, (c) $\Delta x = 0.0025$ m, and (d) $\Delta x = 0.00125$ m.

This treatment of body force assumes that it changes in both space and time, however in the present case uniform force density is applied throughout. Although both models have the same order [$O(2)$] of discretization in space-time, the order of velocity discretization is different [$O(1)$ in [22] and $O(2)$ in [23]]. Thus, two schemes have been implemented: (i) BGK-F1: the BGK collision operator with the force scheme from [22], and (ii) MRT-F2: the MRT operator with the force scheme from [23]. From a computational perspective, the operator BGK is simpler than MRT and the force scheme of [22] is simpler than that of [23]. An analysis of both schemes has been performed for a two-dimensional study, and BGK-F1 is used for a three-dimensional simulation.

The VOF-based mesoscopic advection method [19] is used to identify the motion of the free surface (see Appendix B for details). At the free surface, missing gas nodes are reconstructed using the model of Korner *et al.* [14] to balance the fluid pressure between air and water (see Appendix C for details). The second-order halfway bounce back scheme [29] has been implemented for the side walls and the obstacles.

The presence of a gate to retain the water column at the initial stage of the experiment has been discarded, as its effect on the water column is negligible provided the rising speed of the gate is considerably high [5].

III. NUMERICAL RESULTS

Water is the working fluid for all the test cases carried out in this study. The density of water is taken as $\rho = 10^3$ kg m⁻³ and kinematic viscosity as $\nu = 8.9 \times 10^{-7}$ m² s⁻¹. The gravitational constant g takes a value of 9.81 ms⁻².

A. Dam break impact on a vertical plane wall

A simulation of dam break flow over a dry bed was carried out in accordance with the experimental setup of [5] so as to understand the dynamic pressures imparted on the wall. Five pressure sensors were placed at the locations 0.003, 0.015, 0.03, and 0.08 m on the left wall (Fig. 1). The simulation was performed with two initial filling heights of

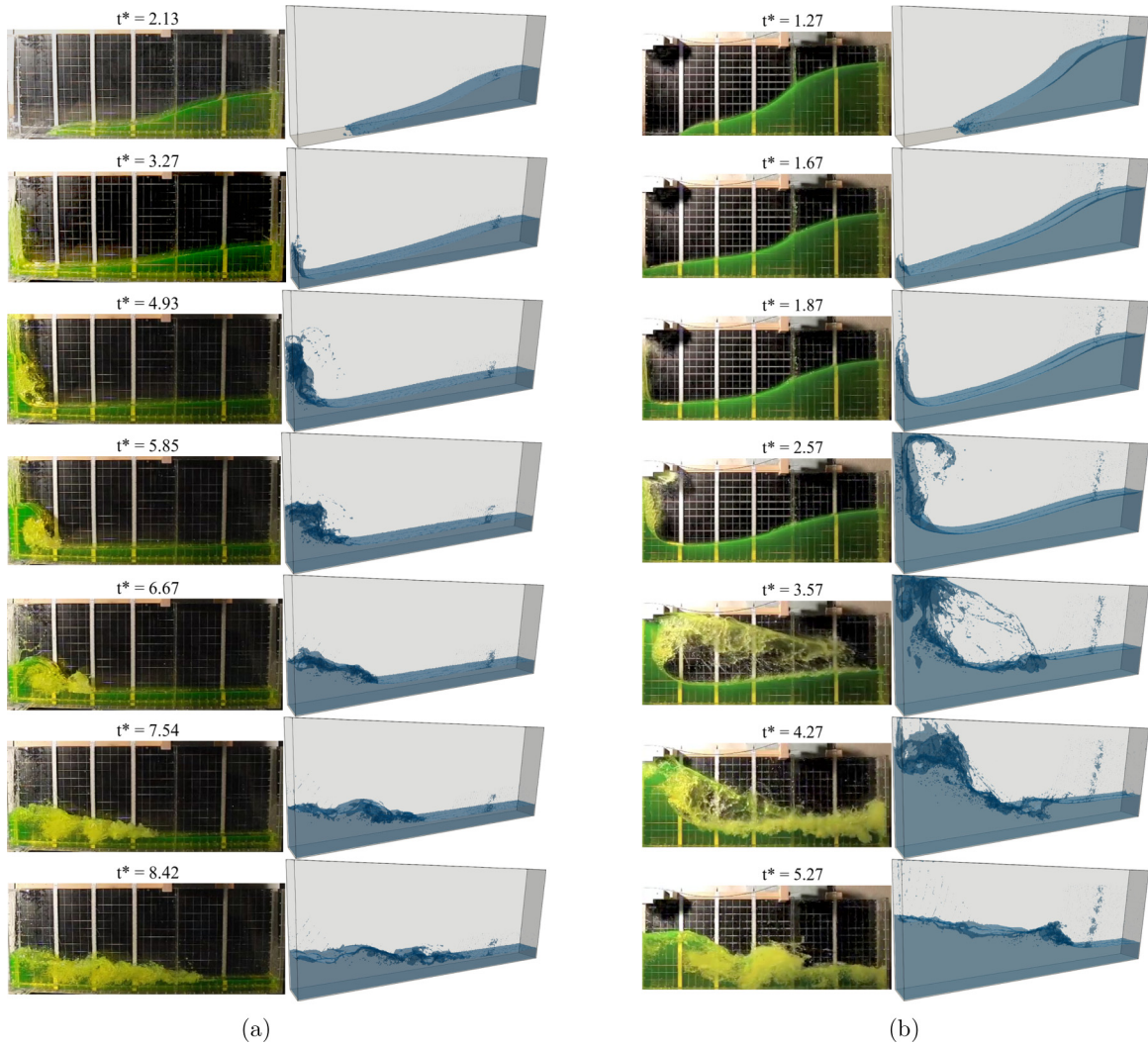


FIG. 3. Comparison of 3D free surface evolution (BGK-F1) with experiment [5]: (a) $H = 0.3$ m and (b) $H = 0.6$ m.

0.3 and 0.6 m with the corresponding Reynolds numbers ($Re = \frac{2A\sqrt{gH}}{\nu}$, where A is the distance between the left wall and the gate, which retains the water column) being 3.8×10^6 and 5.5×10^6 , respectively. A two-dimensional simulation was carried out for the filling height of 0.3 m using BGK-F1 and MRT-F2 schemes. Three grids—coarse, medium, and fine—of size $\Delta x = 0.005, 0.0025,$ and 0.00125 m, respectively, are used to study the effects of grid size in order to establish the grid convergence for each scheme. The corresponding time steps Δt for coarse, medium, and fine grids are $7.29 \times 10^{-5}, 1.46 \times 10^{-6},$ and 3.64×10^{-5} s, respectively. The 3D simulation with the BGK-F1 scheme was carried out using coarse and medium grid sizes. The simulation for $H = 0.6$ m was performed with a medium grid for BGK-F1 and MRT-F2 in 2D and BGK-F1 for the 3D case with $\Delta t = 5.15 \times 10^{-5}$ s. The length (x) and time (t) scales are normalized by H and $\sqrt{g/H}$, respectively ($x^* = x/H$ and $t^* = t\sqrt{g/H}$).

The free surface profile of the 2D simulation using three grid sizes for the BGK-F1 and MRT-F2 schemes at different time steps is shown in Fig. 2. No significant variation has been observed until the flow comes in contact with the wall,

but the shape of the wave tip shows minor variation. In the experiments, the rise of the water column on the left wall has reached the roof, but among the three grids only the finer grid simulation of MRT-F2 reaches the top with the emergence of multiple drops (see $t^* = 3.27$ and 4.93 in Fig. 2). After impingement, the fall back of the water column shows a significant variation in the surface profile (see $t^* = 5.85$ in Fig. 2), especially the shape of plunging. This overturning wave profile shows a large variation in terms of local curvature, and there exists no common pattern that depends on the grid sizes. For example, at $t^* = 5.85$, coarse resolution overturning the profile from BGK-F1 is in the form of a big blob, whereas for medium and fine grids, a smooth overturning exists.

The 3D free surface profile for $H = 0.3$ m shows the three-dimensional features involved in the flow [Fig. 3(a)]. The 3D effects are more apparent after $t^* > 3.97$ when the waterfront hits the wall and the subsequent collapse [Fig. 3(a)]. The profile for fill-level $H = 0.6$ m describes two major event: the impact at the roof and the subsequent splash-up mechanism [Fig. 3(b)]. The major difference in the splash-up is that the observed splash in the experiment [5] was so strong that it

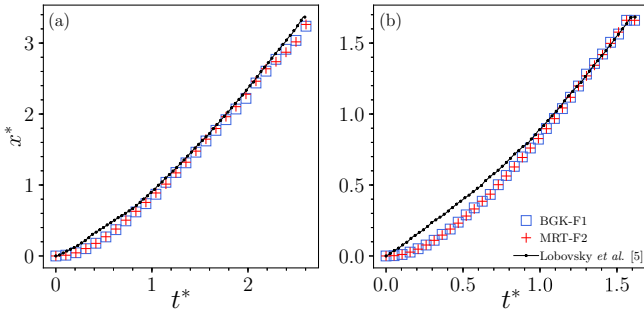


FIG. 4. Time evolution of water front compared with experimental measurements [5] (a) $H = 0.3$ m (results of other grid sizes can be found in the supplemental material [32]) and (b) $H = 0.6$ m.

reached the right wall, whereas the simulation splash did not reach beyond the middle of the tank. This shows that the reflected momentum was not sufficient in the simulation.

The time evolution of the wavefront for 2D simulation is shown in Fig. 4. The convergence of wavefront evolution for each scheme has been verified through computation of the relative error using the L^2 norm, $\|E\|_2 = \sqrt{\frac{\sum_r (x_{G1}^* - x_{G2}^*)^2}{\sum_r (x_{G1}^*)^2}}$, where x_{G1}^* and x_{G2}^* denote the numerical results obtained using grids 1 and 2, respectively. The relative norms for coarse and medium grids of BGK-F1 are 8.5% and 5%, respectively, with reference to the fine grid, and for MRT-F2 they are 6.9% (coarse) and 3.2% (medium). Thus, the decrease in the L^2 norm with an increase in grid size indicates the convergence of the LB models. The evolution of the wavefront for $H = 0.6$ m is not so fast until $t^* < 1$, but it eventually coincides closely with the experiments [5]. This is partly attributed to the gate removal mechanism. On the other hand, in 3D simulation after $t^* > 1$, the increase in velocity results in a faster movement, i.e., the time taken for the water front to impact on the wall after its release is less. The comparison of wavefront evolution obtained from other experimental results [2,5,30] is plotted in Fig. 5(c), ensuring that the results are in agreement.

The average wavefront celerity (nondimensionalized by \sqrt{gH}) is computed for time $t^* > 1$ until the water front hits the wall. The corresponding estimates are given in Table I. The theoretical nondimensional celerity is 2 (since $v = 2\sqrt{gH}$) [5,31], and none of the results has reached this value,

including the experimental measurements [5]. Though the obtained celerity has been consistent with the measurements [5], BGK-F1 shows an increasing trend with an increase in grid size; however, this trend is not observed in MRT-F2.

Pressure is the key hydrodynamic parameter for the impact flows, both peak pressure as well as the duration of the impact event, which plays a major role in the structural safety. Out of five pressure sensors, four (**P1** – **P4**) are placed in line, and **P5** is placed parallel to **P2** to identify the 3D effects [Fig. 1(b)]. Figure 6 shows the results of the comparison of pressure time histories obtained from 2D simulation and the measurements [5]. The first sensor **P1**, which is the first to receive the full impact, is the point of interest, where the prediction of the peaks from BGK-F1 is in agreement with the measurements [5], whereas the MRT-F2 predicts almost twice the measured peak value. A similar trend is observed for sensor **P2** with a major difference observed during the impact. The experimental measurements [5] show a longer duration of impact than the simulation. The 3D effects are observed from the time histories of **P5** while comparing to **P2**, in particular at $t^* = 2.8$ [Fig. 7(a)]. The pressures falls to zero describing the air phase; however, the same is not observed in **P2**, where the continuous profile of water rise exists. The pressure time histories of three-dimensional simulation for $H = 0.6$ m are more consistent with measurements, and there are no secondary peaks as observed in 2D simulation [Fig. 7(b)]. For $H = 0.6$ m, 3D simulation yields higher estimates than 2D. But on the other hand, the pressure peaks from 2D and 3D simulations of $H = 0.3$ m exhibit little variation except for the nondimensional time lag of around 0.1.

B. Three-dimensional dam break impact on a container

A model experiment on the dam break impact on a container was conducted by Maritime Research Institute Netherlands (MARIN) to study the green water effects on the deck of a ship [20]. A tank of dimensions 3.22 m × 1.0 m × 1.0 m was used, with water filled to a depth of 0.55 m on the right side of the tank. The rectangular obstacle placed in front of the water column represents a container placed on the top of a ship’s deck (Fig. 8). A grid spacing of $\Delta x = 6.65 \times 10^{-3}$ m with a time step size of $\Delta t = 10^{-4}$ s was chosen, and the simulation was carried out for a duration of 3 s, during which the flow reached back to the right side of the tank.

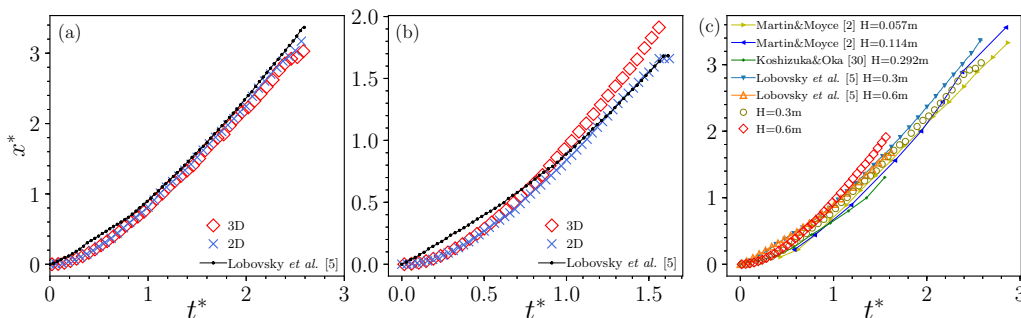


FIG. 5. Time evolution of water front (BGK-F1) compared with experimental measurements [5] (a) $H = 0.3$ m (results of other grid sizes can be found in the supplemental material [32]), (b) $H = 0.6$ m, and (c) evolution profile from other experiments [2,5,30] along with both fill levels used in the present study.

TABLE I. Wavefront celerity.

H (m)	Δx (m)	MRT-F2 (2D)	BGK-F1 (2D)	BGK-F1 (3D)	Experiment [5]
0.3	0.005	1.74	1.55	1.57	1.56
	0.0025	1.53	1.58	1.59	
	0.00125	1.57	1.60		
0.6	0.0025	1.36	1.45	1.46	1.34

The free surface evolution shows that the simulation captured two basic flow features during the impact: (i) the immediate generation of splash-up, and (ii) the rise of a vertical jet over the container (Fig. 9). Both observations are similar to that of an experiment [20]. The subsequent mechanism of rising vertical jets over the wall and the secondary flow, which impacts the container’s backface, are also in agreement. The height of the vertical jet reaches only about half of the tank’s height, but in another simulation [9] the jet reached the roof of the tank. The water level measurements are taken at two locations: one in the middle of the water column (**H2**) and the other in front of the container (**H4**) [Fig. 8(a)]. During the secondary flow, probe **H2** shows a different feature compared to that of the measurements [20], wherein a

comparable increase in the water level was observed at $t = 1.4$ s (Fig. 10). The rate of decrease in the water level shows a good agreement with the measurements [20], but the gap after $t > 2.5$ s was because of the delayed capturing of secondary flow.

A comparison of pressure time histories reveals that LB prediction is on par with the measurements except near the aerated region. This fact can be seen from the time series of probes **P1** and **P3** located in front of the container, where LB results are matched with the measurements [20] until 1.5 s, and at a later duration the oscillatory behavior of pressure has been observed, which is due to the presence of aerated water (Fig. 11). The probes **P5** and **P7** on the top of the wall reveal an oscillatory pattern of pressure right from the first point of

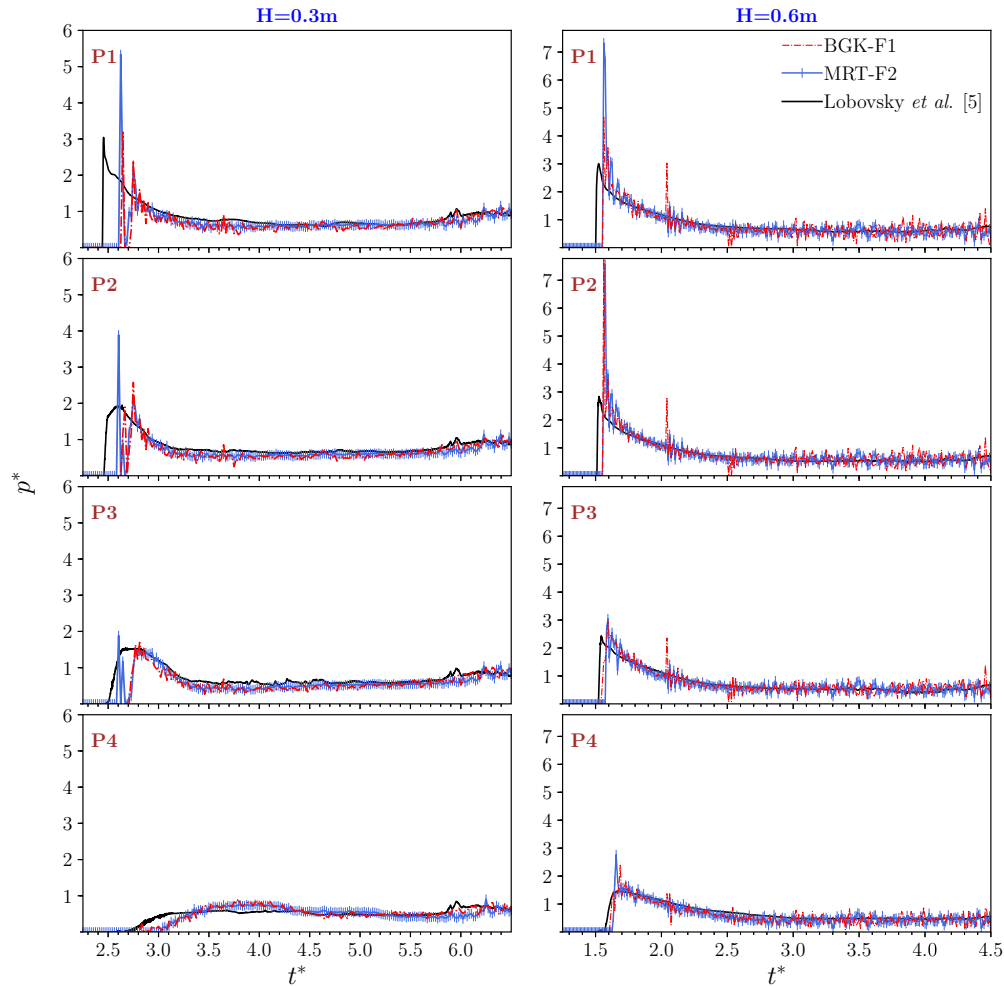


FIG. 6. Comparison of pressure time histories for 2D simulation $H = 0.3$ m (left) (results of other grid sizes can be found in the supplemental material [32]) and $H = 0.6$ m (right).

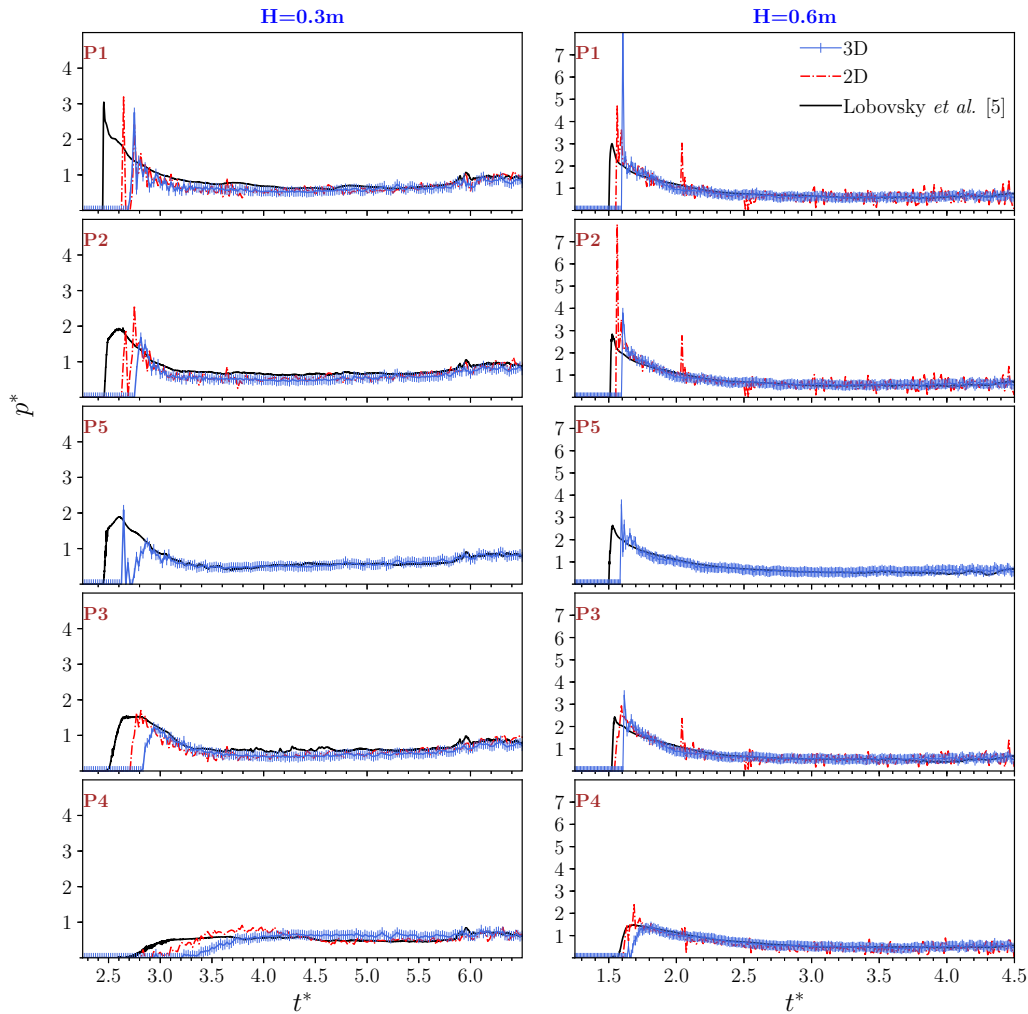


FIG. 7. Comparison of pressure time histories for 3D simulation along with 2D BGK-F1 time histories $H = 0.3$ m (left) (results of other grid sizes can be found in the supplemental material [32]) and $H = 0.6$ m (right).

impact, and in addition the pressure peaks are underestimated. In comparison to the NS-VOF solution of [20] (see Fig. 20 in Ref. [20]), the intermediate pressure spikes attributed to the discontinuities in the cell conversion have not been found in the present LBM, yet the overall trend matches with the measurements [20].

C. Three-dimensional dam break impact on a tall structure

In contrast with the previous two test cases, the presence of a wet-bed and a tall tower relative to the height of the water column make the case of impact on a tall structure

more relevant in the context of coastal and ocean engineering, because when the water column is released, the waterfront pushes the water-bed, which results in a wakelike flow. The experimental setup consists of a water tank of dimensions $1.6 \text{ m} \times 0.61 \text{ m} \times 0.75 \text{ m}$ with a water-bed of depth 0.01 m , and a tall tower of dimensions $0.12 \text{ m} \times 0.12 \text{ m} \times 0.75 \text{ m}$ that was placed at a distance of 0.5 m from the water column (Fig. 12). The height of the computational domain is reduced to 0.65 m to avoid an increase in computational cost [33]. The values of Δx and Δt are chosen as 0.004 m and $8.16 \times 10^{-5} \text{ s}$, respectively. The simulation is carried out for a duration of 3 s . The available experimental measurements for this test case are

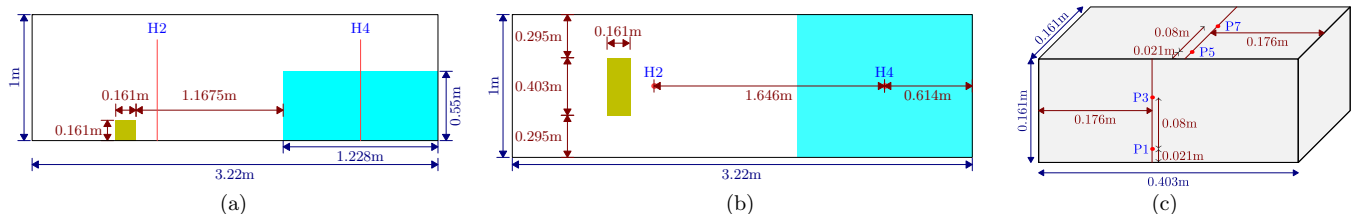


FIG. 8. Initial dam break setup [20]: (a) side view, (b) top view, and (c) obstacle.

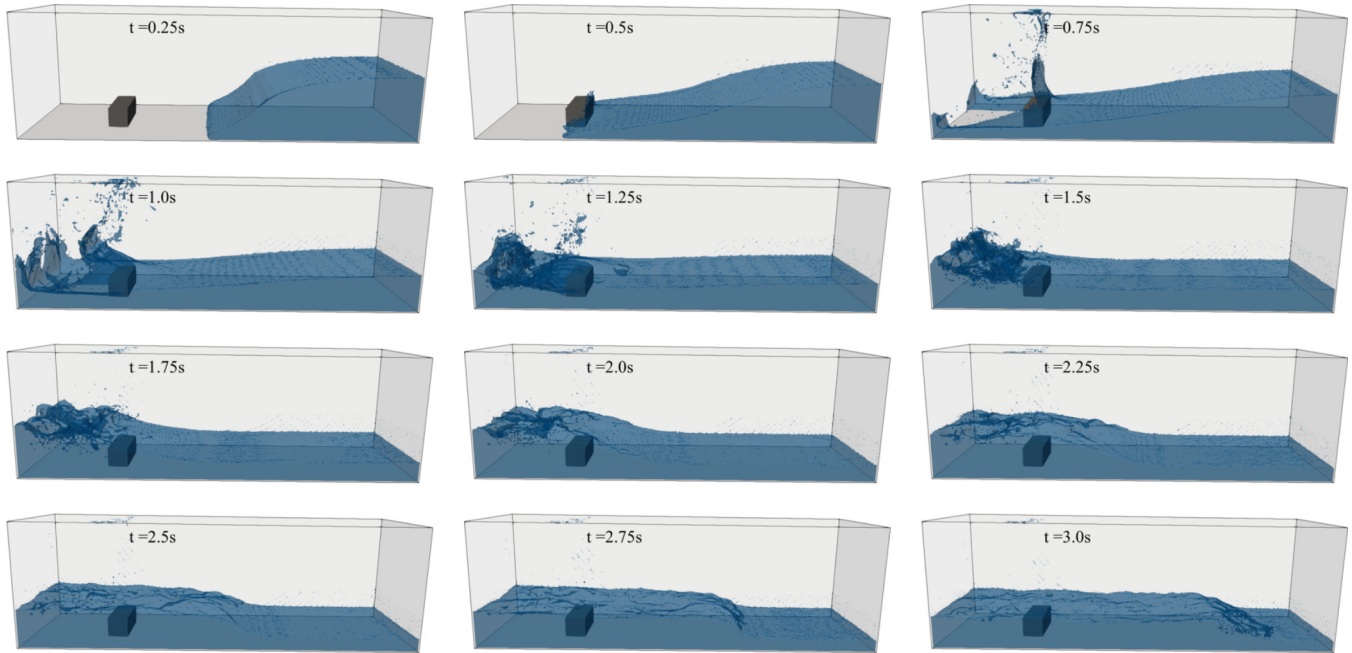
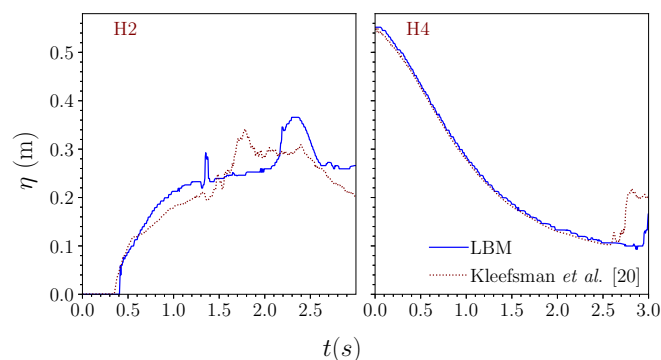


FIG. 9. Free surface evolution of dam-break flow impact on the container.

as follows: time histories of horizontal velocity obtained at the location (0.754, 0.31, 0.026) and the net horizontal force imparted on the structure.

The evolution of a free surface at various time steps is given in Fig. 13, and two time instants are of interest: (i) $t = 0-0.6$ s, the initial impact and the occurrence of maximum force, and (ii) $t = 0.87-1.75$ s, the reflected wave from the wall, which hits the rear side of the tower, resulting in negative force. The wave form can be visible at a time $t = 0.25$ s, and upon hitting the tower the maximum level that the water reaches is less than half of the tank's height. The emergence of multiple droplets can be observed, and one such group travels to the top of the tank. The total duration was found to be 0.57 s from the time the droplets break until they merge with the bottom (see time steps $t = 0.36-1.0$ s in Fig. 13). Since experimental videos and photographs are not available, it is difficult to quantify how many such droplets (volume of water) had emerged, and their duration before their merging. It should be noted that there was no occurrence of drops when the reflected wave impinged the tower.

FIG. 10. Evolution of water level at probes **H2** and **H4** for dam break impact on a container.

A comparison of time histories reveals that the waterfront reaches the tower much faster in the simulation than in the experiment [21]. This might be due to two reasons: first, there is no gate opening mechanism involved in the simulation, and second, the presence of a wet-bed that receives constant body force would gain significant momentum, yielding the positive force (Fig. 14). Though the peak velocity from the simulation is higher than the experiment, the overall trend is in agreement with the measurements. The velocity values during $t = 2.529-2.856$ s are negligible because of the occurrence of air-entrapment due to the plunging wave [Fig. 14(a)]. This duration of 0.327 s cannot be inferred from the experimental values [21], yet the numerical investigations conducted earlier [33] show that the breaking was indeed plunging. This further justifies the relevance of the present case in ocean engineering problems.

Two peak forces are observed during the primary wave impact at $t = 0.27$ and 0.39 s [Fig. 14(b)]. The first occurrence is attributed to the impact of the wave tip so formed after the initial entrapment of air and second peak at the aftermath of the complete collapse of the entrapped air. The calculation of force impulse reveals the deviations and errors that arise at the initial stages of the force calculation, and they prove to be much more sensitive than the actual force. Figure 14(c) shows a comparison of force impulse and the observed deviation at around 0.5 s, which is attributed to the second peak of the primary flow. The secondary flow, which is still active, continues to impart a negative force on the tower. The sharp decay shows that the flow approaches equilibrium until the water becomes calm.

IV. SUMMARY AND CONCLUSIONS

In this study, the load estimates due to dam break impact flows have been studied using the free surface lattice Boltzmann method. A two-dimensional simulation using BGK and

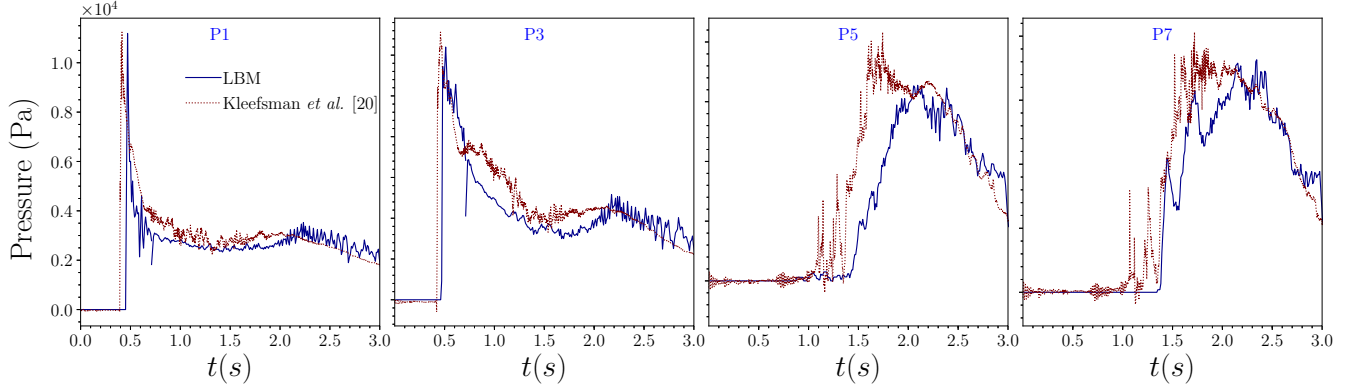


FIG. 11. Comparison of pressure time histories for dam break impact on a container.

MRT schemes with the respective force schemes of [22] (BGK-F1) and [23] (MRT-F2) was performed. BGK-F1 is found to perform better in the context of pressure evaluation, even though the free surface evolution, waterfront celerity, and its evolution do not show any significant variations between them. Thus, if the body force is uniform, then BGK-F1 results in a good estimate of pressure for the free surface problems. The existence of an air phase on one side of the wall and the water on the other illustrates the 3D characteristics, and it has been observed from the pressure history of a simulation of dam break impact on the wall. The major drawback noticed from the free surface evolution is that in all three cases after impingement on the wall, the momentum was not significant to cope with the experiments.

Overall, the simulation results are in good agreement with the measurements, thus enhancing further interest in the improvements required for the LBM. Since the LBM belongs to the mesoscale modeling approach, in the present study the prediction of a macroscale property such as pressure proves that the free surface LBM indeed requires further extensions in order to prove itself as a strong contender for CFD applications, especially (i) improved wall boundary conditions in the aerated water regions, and (ii) rectangular and nonuniform grids to handle the complex interface geometry.

APPENDIX A: LES TURBULENCE MODEL

In the LES models, the eddy viscosity ν_{eddy} has been added to the molecular viscosity ν to take care of additional

fluctuations related to the viscous layer. In the present context, the relaxation time τ in the collision operator Λ , which is directly related to ν , is decomposed into two relaxation times, τ_ν and τ_{eddy} . Thus, $\tau = \tau_\nu + \tau_{\text{eddy}}$ with $\tau_\nu = 3\nu + 0.5$ and $\tau_{\text{eddy}} = 3\nu_{\text{eddy}}$, where τ_ν is related to the actual viscosity of the fluid and τ_{eddy} to the turbulent eddy viscosity. The Smagorinsky model for LES is used in the present study, in which ν_{eddy} is related to the shear-rate tensor $\bar{\mathbf{S}}$,

$$\nu_{\text{eddy}} = (C_{\text{sgs}} \bar{\Delta})^2 \sqrt{2\bar{\mathbf{S}}_{\alpha\beta} \cdot \bar{\mathbf{S}}_{\alpha\beta}}, \quad (\text{A1})$$

where C_{sgs} is the Smagorinsky constant, $\bar{\Delta}$ is the filter length, and $\bar{\mathbf{S}}_{\alpha\beta} = \frac{1}{2}(\partial_\alpha u_\beta + \partial_\beta u_\alpha)$. Based on Chapman-Enskog expansion analysis, second-order moments of the LB distribution function approximate the momentum flux tensor of the NS equation [34]. Thus, $\bar{\mathbf{S}}_{\alpha\beta}$ is related to the nonequilibrium momentum flux tensor, which in turn proved to be an advantage as the computation of derivatives can now be performed locally,

$$\bar{\mathbf{S}}_{\alpha\beta} = \frac{-3}{2\rho(\tau_\nu + \tau_{\text{eddy}})} \Pi_{\alpha\beta}, \quad (\text{A2})$$

with $\Pi_{\alpha\beta} = \sum_\gamma \mathbf{e}_{\gamma\alpha} \mathbf{e}_{\gamma\beta} (f_\gamma - f_\gamma^{\text{eq}})$. Using Eqs. (A1) and (A2), the expression for τ_{eddy} be written as

$$\begin{aligned} \tau_{\text{eddy}} &= 3(C_{\text{sgs}} \bar{\Delta})^2 \sqrt{2\bar{\mathbf{S}}_{\alpha\beta} \cdot \bar{\mathbf{S}}_{\alpha\beta}} \\ &= \frac{9}{2} \frac{(C_{\text{sgs}} \bar{\Delta})^2}{\rho(\tau_\nu + \tau_{\text{eddy}})} \sqrt{2\Pi_{\alpha\beta} \cdot \Pi_{\alpha\beta}}. \end{aligned} \quad (\text{A3})$$

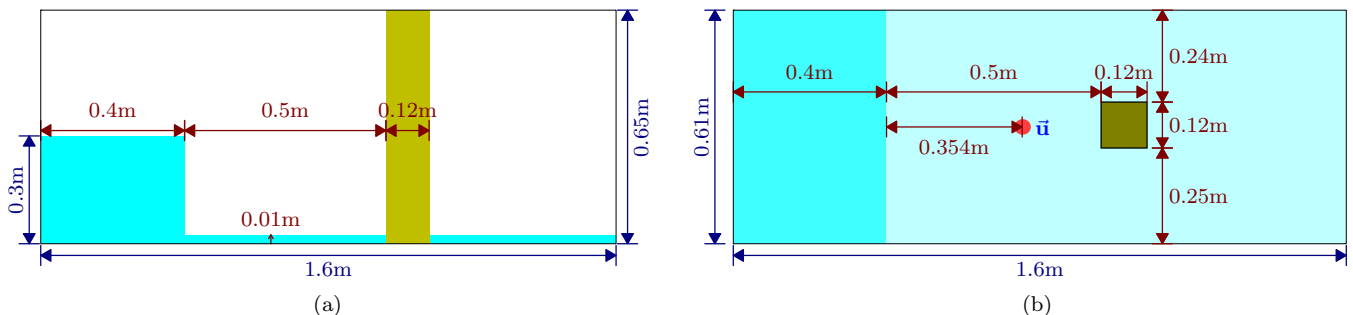


FIG. 12. Initial dam break setup [21]: (a) side view and (b) top view.

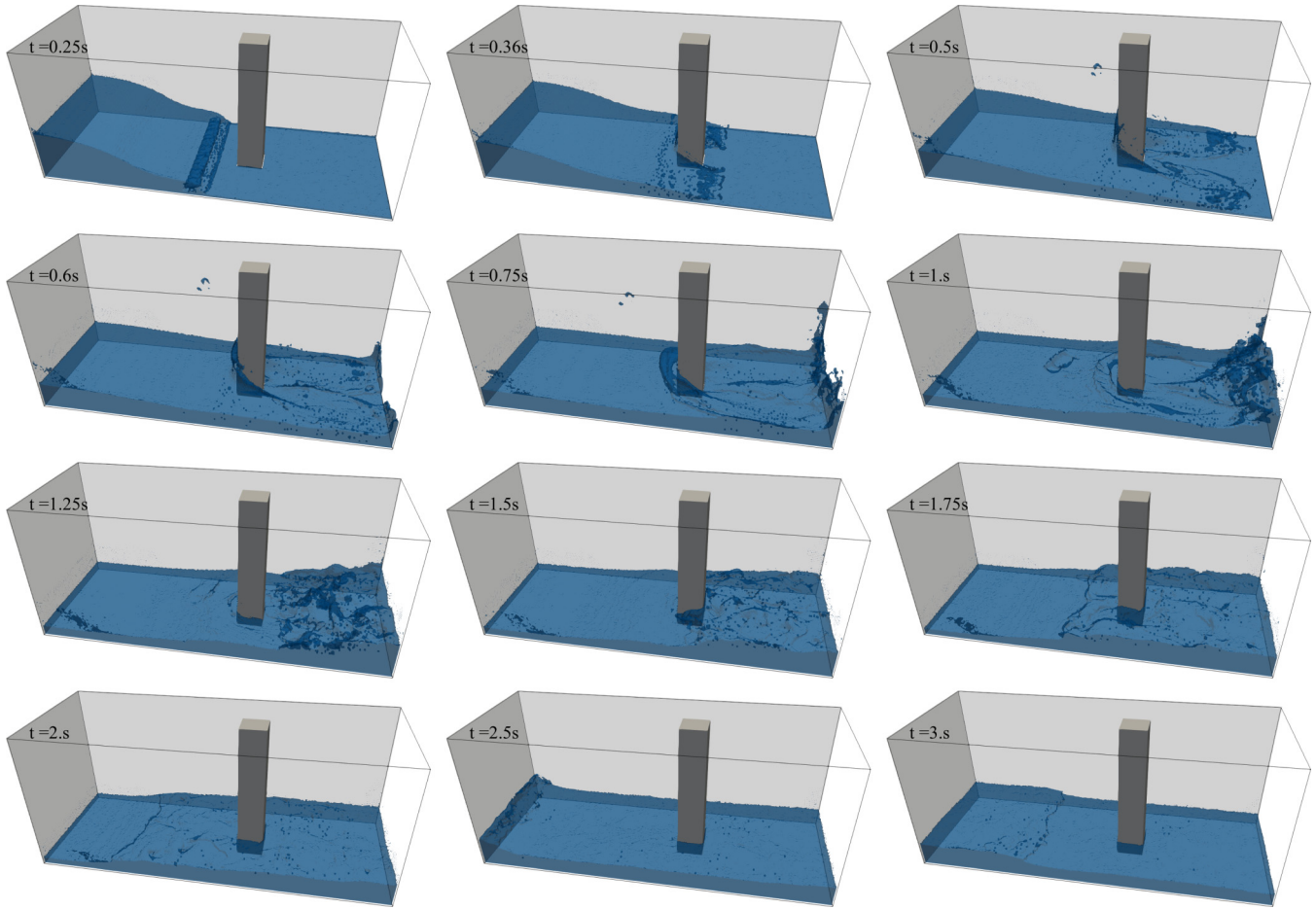


FIG. 13. Free surface evolution of dam-break flow impact on the tower.

Finally, the expression for relaxation time related to eddy viscosity τ_{eddy} can be obtained by solving the quadratic equation (A3),

$$\tau_{\text{eddy}} = \frac{1}{2} \left[-\tau_v + \sqrt{\tau_v^2 + 18 \frac{(C_{\text{sgs}} \bar{\Delta})^2}{\rho} \sqrt{2\Pi_{\alpha\beta} \cdot \Pi_{\alpha\beta}}} \right]. \tag{A4}$$

APPENDIX B: FREE SURFACE MODEL

In volume of fluid (VOF) -based schemes, computational nodes are identified by the fluid fraction (or fill-level) variable ϵ , which represents the amount of liquid contained in the cell and is defined by the ratio of mass to density. Thus, $\epsilon = 1$ represents a liquid node, $\epsilon = 0$ represents gas, and at the interface node ϵ takes a value between 0 and 1. The evolution

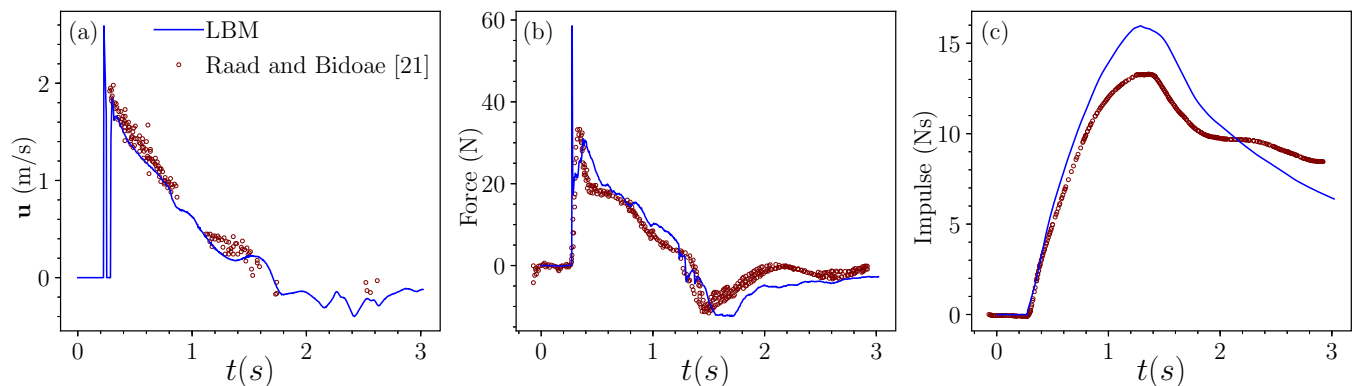


FIG. 14. Comparison between LB and experimental measurements [21]: (a) velocity probe in front of the structure, (b) force exerted on the obstacle, and (c) cumulative impulse.

of ϵ is governed by the advection equation

$$\frac{\partial \epsilon}{\partial t} + \mathbf{u} \cdot \nabla \epsilon = \mathbf{0}. \quad (\text{B1})$$

In the present study, a geometry-based mesoscopic advection method [15] is used to solve Eq. (B1), though one can use the traditional discretization schemes as well [12]. At first, the evaluation of mass flux ϕ_i is computed as

$$\phi_i(\mathbf{x}, t) = A_i(\mathbf{x}, t) \cdot [f_{-i}(\mathbf{x}, t) - f_i(\mathbf{x}, t)], \quad (\text{B2})$$

where f_{-i} and f_i represent the distribution functions that enter and leave the node at \mathbf{x} in the i th direction, respectively, and

$$A_i(\mathbf{x}) = \begin{cases} 1 & \text{if } \mathbf{x} + \mathbf{e}_i \text{ is liquid,} \\ 0 & \text{if } \mathbf{x} + \mathbf{e}_i \text{ is gas,} \\ \frac{\epsilon(\mathbf{x}) + \epsilon(\mathbf{x} + \mathbf{e}_i)}{2} & \text{if } \mathbf{x} + \mathbf{e}_i \text{ is interface.} \end{cases} \quad (\text{B3})$$

The estimation of the fill level from Eq. (B3) does not require any construction of surface normal and its gradient as compared to the initially proposed VOF-PLIC [12]. Even though a fairly accurate representation of the free surface can be obtained from this model, few improvements on free surface modeling have been proposed, viz., VOF-PLIC [15], the front-tracking method [35], and a level set [36]. Furthermore, the present scheme has been chosen for its simplicity in handling the free surface computation compared with the other methods. The evolution of mass m is then described by

$$\frac{\partial m}{\partial t} + \sum_i \phi_i = 0. \quad (\text{B4})$$

The discretization of Eq. (B4) using Euler's forward difference scheme leads to

$$m(\mathbf{x}, t + \Delta t) = m(\mathbf{x}, t) - \Delta t \sum_i \phi_i(\mathbf{x}, t). \quad (\text{B5})$$

Thus, the update rule for ϵ can be written as

$$\begin{aligned} \epsilon(\mathbf{x}, t + \Delta t) &= \frac{m(\mathbf{x}, t + \Delta t)}{\rho(\mathbf{x}, t + \Delta t)} \\ &= \frac{m(\mathbf{x}, t) - \Delta t \sum_i \phi_i(\mathbf{x}, t)}{\rho(\mathbf{x}, t + \Delta t)} \\ &= \frac{\epsilon(\mathbf{x}, t) \rho(\mathbf{x}, t) - \Delta t \sum_i \phi_i(\mathbf{x}, t)}{\rho(\mathbf{x}, t + \Delta t)}. \end{aligned} \quad (\text{B6})$$

The present method is referred as an *unsplit method* as the computation of mass flux in all directions has been treated simultaneously [15].

APPENDIX C: FREE SURFACE BOUNDARY CONDITION

In free surface problems, the absence of distribution functions for the gas node poses a difficulty in performing the streaming step, as each liquid or interface node must receive the DF's from the neighboring nodes. Thus, the reconstruction of missing DF's should satisfy the following boundary conditions at the interface: (i) liquid and gas nodes on the interface must travel with the same velocity, and (ii) forces exerted between them must be balanced. To pass the interface node, the velocity of gas nodes must be directed inward, and hence the missing DF can be written as [14]

$$\begin{aligned} f_i(\mathbf{x} - \mathbf{e}_i \Delta t, t) &= f_i^{\text{eq}}(\rho_{\text{atm}}, \mathbf{u}) + f_{-i}^{\text{eq}}(\rho_{\text{atm}}, \mathbf{u}) - f_{-i}(\mathbf{x}, t) \\ &\text{if } \mathbf{n} \cdot \mathbf{e}_i \geq 0, \end{aligned} \quad (\text{C1})$$

where ρ_{atm} refers to the atmospheric gas density, and it takes the same value of density used in the simulation. The normal vector \mathbf{n} can be obtained from the derivative of the fluid fraction ϵ as $\mathbf{n} = \frac{\mathbf{v}_\epsilon}{\|\nabla \epsilon\|}$.

-
- [1] P. A. Tyvand, K. M. Solbakken, and K. B. Hjelmervik, *Eur. J. Mech. B/Fluids* **47**, 202 (2014).
- [2] J. C. Martin, W. J. Moyce, W. G. Penney, A. Price, and C. Thornhill, *Philos. Trans. R. Soc. London, Ser. A* **244**, 312 (1952).
- [3] R. F. Dressler, *Int. Assoc. Sci. Hydrology* **3**, 319 (1954).
- [4] M. A. Cruchaga, D. J. Celentano, and T. E. Tezduyar, *Comput. Mech.* **39**, 453 (2007).
- [5] L. Lobovsky, E. Botia-Vera, F. Castellana, J. Mas-Soler, and A. Souto-Iglesias, *J. Fluids Struct.* **48**, 407 (2014).
- [6] A. Korobkin and O. Yilmaz, *J. Eng. Math.* **63**, 293 (2009).
- [7] J. J. Stoker, *Water Waves: The Mathematical Theory with Applications* (Wiley, New York, 2011), Vol. 36.
- [8] A. Colagrossi and M. Landrini, *J. Comput. Phys.* **191**, 448 (2003).
- [9] V.-T. Nguyen and W.-G. Park, *Int. J. Numer. Meth. Fluids* **82**, 3 (2016).
- [10] L. Luo, M. Krafczyk, and W. Shyy, Lattice Boltzmann method for computational fluid dynamics, *Encyclopedia of Aerospace Engineering*, edited by R. Blockley and W. Shyy (Wiley, 2010).
- [11] G. Tryggvason, B. Bunner, A. Esmaeeli, D. Juric, N. Al-Rawahi, W. Tauber, J. Han, S. Nas, and Y.-J. Jan, *J. Comput. Phys.* **169**, 708 (2001).
- [12] C. W. Hirt and B. D. Nichols, *J. Comput. Phys.* **39**, 201 (1981).
- [13] S. Osher and R. Fedkiw, *Level Set Methods and Dynamic Implicit Surfaces* (Springer Science & Business Media, New York, 2006), Vol. 153.
- [14] C. Körner, M. Thies, T. Hofmann, N. Thürey, and U. Rüde, *J. Stat. Phys.* **121**, 179 (2005).
- [15] C. F. Janßen, S. T. Grilli, and M. Krafczyk, *Comput. Math. Appl.* **65**, 211 (2013).
- [16] S. Bogner, J. Harting, and U. Rüde, *Int. J. Comput. Fluid Dyn.* **31**, 463 (2017).
- [17] X. Q. Xing, D. L. Butler, and C. Yang, *Int. J. Numer. Meth. Fluids* **53**, 333 (2007).
- [18] Z. Zhao, P. Huang, Y. Li, and J. Li, *Int. J. Numer. Meth. Fluids* **71**, 223 (2013).
- [19] C. F. Janßen and M. Krafczyk, *Comput. Math. Appl.* **61**, 3549 (2011).
- [20] K. Kleefsman, G. Fekken, A. Veldman, B. Iwanowski, and B. Buchner, *J. Comput. Phys.* **206**, 363 (2005).
- [21] P. E. Raad and R. Bidoae, *J. Comput. Phys.* **203**, 668 (2005).
- [22] J. M. Buick and C. A. Greated, *Phys. Rev. E* **61**, 5307 (2000).
- [23] Z. Guo, C. Zheng, and B. Shi, *Phys. Rev. E* **65**, 046308 (2002).
- [24] T. Krüger, H. Kusumaatmaja, A. Kuzmin, O. Shardt, G. Silva, and E. M. Vigen, *The Lattice Boltzmann Method* (Springer International Publishing, Switzerland, 2017).

- [25] M. Krafczyk, J. Tölke, and L.-S. Luo, *Int. J. Mod. Phys. B* **17**, 33 (2003).
- [26] C. Zhang, Y. Cheng, S. Huang, and J. Wu, *Adv. Appl. Math. Mech.* **8**, 145 (2016).
- [27] C. Shu, X. Niu, Y. Chew, and Q. Cai, *Math. Comput. Simul.* **72**, 201 (2006).
- [28] H. Yu, L.-S. Luo, and S. S. Girimaji, *Comput. Fluids* **35**, 957 (2006).
- [29] M. Bouzidi, M. Firdaouss, and P. Lallemand, *Phys. Fluids* **13**, 3452 (2001).
- [30] S. Koshizuka and Y. Oka, *Nucl. Sci. Eng.* **123**, 421 (1996).
- [31] A. Ritter, *Vereine Deutcher Ingenieure Zeitschrift* **36**, 947 (1892).
- [32] See Supplemental Material at <http://link.aps.org/supplemental/10.1103/PhysRevE.99.023308> for convergence results of different grid sizes..
- [33] M. Gómez-Gesteira and R. A. Dalrymple, *J. Waterway Port Coast. Ocean Eng.* **130**, 63 (2004).
- [34] T. Krüger, F. Varnik, and D. Raabe, *Phys. Rev. E* **79**, 046704 (2009).
- [35] P. Lallemand, L.-S. Luo, and Y. Peng, *J. Comput. Phys.* **226**, 1367 (2007).
- [36] U. Rüde and N. Thürey, Free surface lattice-Boltzmann fluid simulations with and without level sets, in *Proceedings of Vision, Modeling and Visualization* (IOS Press, 2004), pp. 199–208.